IEEE Access
Multidisciplinary ⋮ Rapid Review ⋮ Open Access Journal

Received April 28, 2022, accepted May 10, 2022, date of publication May 16, 2022, date of current version May 23, 2022.

Digital Object Identifier 10.1109/ACCESS.2022.3175311

Pneumothorax Recognition Neural Network Based on Feature Fusion of Frontal and Lateral Chest X-Ray Images

JIA XIN LUO[1], WU FENG LIU[2], AND LIANG YU[1]
[1]College of Electrical Engineering, Henan University of Technology, Zhengzhou 450001, China
[2]School of Artificial Intelligence and Big Data, Henan University of Technology, Zhengzhou 450001, China

Corresponding author: Wu Feng Liu (lwf@haut.edu.cn)

This work was supported by the National Natural Science Foundation of China for Young Scholar under Grant 11005136.

ABSTRACT Pneumothorax is a potentially life-threatening disease that requires urgent diagnosis and treatment. Clinically, a chest X-ray examination is the first choice for diagnosing pneumothorax. However, it is difficult to diagnose pneumothorax by only frontal chest X-ray imaging when the lesion area is only composed of a small amount of air. Therefore, we propose a pneumothorax diagnosis neural network based on feature fusion, where frontal and lateral X-ray information are fused. In this network, there are two inputs and three outputs. The two inputs are the frontal chest X-ray image and the lateral chest X-ray image. The three outputs are the classification results of the frontal chest X-ray image, the classification results of the lateral chest X-ray image, and the classification results integrating the characteristics of the fused frontal chest X-ray image and lateral chest X-ray image. Our algorithm considers the vanishing gradient problem in the pneumothorax recognition model and introduces the residual block to alleviate this problem. Because of the large number of channels in this model, we also utilize channel attention mechanisms to improve the model's performance. Our comparative experiments show that neural network fusion of frontal and lateral chest image features can achieve higher accuracy than the single task model. Using only image-level annotation, our pneumothorax model can achieve high recognition accuracy.

INDEX TERMS Convolutional neural network, pneumothorax, chest X-ray images, computer-aided diagnosis, multiple input network.

I. INTRODUCTION

Pneumothorax (lung collapse) occurs when excessive air accumulates in the pleural cavity between the lung and the chest wall. This air pressure causes the lung to collapse. The main symptoms of pneumothorax are chest tightness, shortness of breath, and cough. Pneumothorax may be caused by physical factors, such as chest trauma or impact, smoking, and pulmonary diseases [1], [2]. The diagnosis of pneumothorax is very complex and is usually determined by radiologists based on a chest X-ray examination. However, using a chest X-ray to diagnose pneumothorax is challenging for radiologists. Even experienced radiologists need to carefully adjust image display settings, such as the window width, window level, and image contrast, to make the correct diagnosis of the disease. This work requires a large amount of clinical experience and patience. Sometimes, fatigued doctors will make incorrect judgments. The diagnostic accuracy of pneumothorax highly depends on the expertise of the attending radiologist [3], [4].

In the absence of trained radiologists, the correct diagnosis and treatment of pneumothorax are often delayed, which may cause serious injury or even death in patients. The above situation is common in some undeveloped countries and regions. Therefore, there is an urgent need for a computer-aided diagnostic [5], [6] (CAD) tool to help doctors accurately diagnose and detect pneumothorax. Deep learning-based technology is a popular choice for image segmentation and classification. Great success has been achieved using deep learning in different fields, such as natural scene image understanding [7], geographic exploration [8], and medical image recognition [9], [10]. The popularization of object detection, semantic segmentation, and disease classification based on deep learning has greatly relieved doctors of tedious work

The associate editor coordinating the review of this manuscript and approving it for publication was Kathiravan Srinivasan.

and improved the diagnosis efficiency [11]–[14]. Multitask learning strategies [15], [16], such as Siamese networks [17] and auxiliary tasks [18], have attracted increasing attention in computer-aided diagnostics.

In engineering, when designing an outstanding pneumothorax auxiliary diagnosis algorithm, the following challenges are usually encountered. The resolution of a chest X-ray is limited, and it is difficult to distinguish when the lesion area contains only a small amount of air. Air accumulation areas can be scattered at various locations and appear in multiple shapes. Pixel-level medical image annotation (i.e., strong supervision) is expensive and difficult to obtain. Image level medical image annotation (i.e., weak supervision) is relatively easy to obtain, but it is not easy to use to achieve high recognition accuracy [19].

To alleviate these problems, we propose a multitask learning model [15] (i.e., a fusion model) for the automatic detection of pneumothorax. The model can be used to fuse information from frontal and lateral chest X-ray images to realize high-precision automatic recognition of pneumothorax. We invited experienced radiologists to build a pneumothorax image dataset (Haut-NY). This dataset contains not only frontal chest X-ray images but also corresponding lateral chest X-ray images, which is meaningful. Many well-known pneumothorax datasets, such as the National Institutes of Health chest X-ray dataset [19], [20] and the Society for Imaging Informatics in Medicine (SIIM) Pneumothorax Challenge Dataset [21], do not contain lateral chest X-ray images. The main contributions of this work are summarized as follows.

- Different from previous works that only use frontal chest X-ray images to identify pneumothorax, we propose a multi-input multi-output neural network that can fuse information from frontal and lateral chest X-ray images. Experiments show that the model's accuracy is higher than that of the model using only frontal or lateral chest X-ray images.
- The fusion model includes residual block and channel attention mechanism. The residual block alleviates the vanishing gradient problem, and the channel attention mechanism gives different weights to different feature maps. Experiments show that those strategies can improve the pneumothorax recognition accuracy of the fusion model.
- The fusion model proposed in this paper only needs image-level annotation to achieve high pneumothorax recognition accuracy.

The rest of this study is organized as follows. In Section II, the literature on the automatic diagnosis of pneumothorax is introduced. In Section III, the specific structure and classification results of the fusion model, including the details of the dataset, the hyperparameters, and the comparison with the single input model, are described. In Section IV, a comparison of our model to models from excellent articles in recent years is given. Discussions, conclusions, and future work are given in Sections V and VI.

II. RELATED WORKS

Early automatic pneumothorax detection methods relied on traditional feature extraction techniques. Hough transform [6] was used to model the appearance of pneumothorax in X-ray images and local intensity histograms, image edge detection was used to catch the visceral pleural edge [22], and texture information was used to quantify pulmonary vascular markers [23]. Because the predefined appearance features cannot capture a variety of human lungs and pneumothorax, the diagnostic accuracy of such algorithms is still relatively low. The development of deep learning has introduced a new approach for the automatic diagnosis of pneumothorax. The deep learning algorithm can be used to train the model to classify X-ray images of lungs with pneumothorax and without pneumothorax [24], [25]. Cicero *et al.* [26] pioneered pneumothorax diagnosis. They used GoogLeNet to detect five common lung diseases using more than 35,000 adult chest X-ray images. The accuracy of pneumothorax detection was 0.86 AUC (area under the curve). Taylor *et al.* [27] compared the performance of Inception, VGG, and ResNet neural network architectures, and the AUC obtained for pneumothorax detection was 0.94. Rajpurkar *et al.* [28] later proved that the performance of ResNet is statistically equivalent to the ability of radiologists to diagnose pneumothorax through chest X-ray images. Park applied the YOLO series network to identify traumatic pneumothorax after chest puncture. Wang *et al.* [14] used a multitask training strategy to improve the accuracy of pneumothorax recognition. The AUC obtained in pneumothorax detection was 0.9786. The highest AUC value was achieved by Wang *et al.* [30], who combined medical reports with X-ray images from the same patient to achieve automatic pneumothorax classification. The AUC obtained in pneumothorax detection was 0.995. To protect the privacy of patients, they did not publish these reports.

TABLE 1. Related work on pneumothorax classification in recent years.

Related work	Task	Annotation	AUC
Cicero et al. [26]	Multi-classification	Image level	0.86
Taylor et al. [27]	Binary classification	Image level	0.94
Rajpurkar et al. [28]	Multi-classification	Image level	0.94
Park et al. [29]	Binary classification	Bounding box	0.905
Xiyue Wang et al. [14]	Binary classification	Pixel level	0.9786
Xiaosong Wang et al. [30]	Multi-classification	Medical reports	0.995
Our work	Binary classification	Image level	0.979

III. EXPERIMENTS

A. OBJECTIVES

The work presented in [14] and [30] is better than that of most other work on pneumothorax recognition. The former used pixel-level annotation, while the latter used medical reports to detect pneumothorax. However, these two types of

annotations are expensive. How to use low-cost image-level annotation to achieve high-precision pneumothorax recognition is our main objective. Different sizes of pneumothorax may be presented in the front chest X-ray image and the lateral chest X-ray image of the same patient. Frontal chest X-ray images and lateral chest X-ray images have their own advantages. Therefore, we aim to use a neural network to fuse frontal chest X-ray image information and lateral chest X-ray image information to improve the accuracy of pneumothorax recognition.

B. DATASETS AND DATA ENHANCEMENT METHODS

1) DATASET

In cooperation with Nanyang Central Hospital in Henan Province, China, we collected 2,530 pairs of chest X-ray images from patients of different ages and gender (each pair consists of a frontal and lateral chest X-ray image from the same patient). The dataset contains a total of 5,060 digital imaging and communications in medicine (DICOM) files. Each DICOM file includes the patient's protected health information (PHI), including name, sex, age, and image-related information. Specifically, there were 1,670 negative pneumothorax cases and 860 positive pneumothorax cases, which were labeled by experienced radiologists. Figure 1 shows X-ray images of one patient taken from different angles. The specific data distribution is shown in Figure 2 and Figure 3.

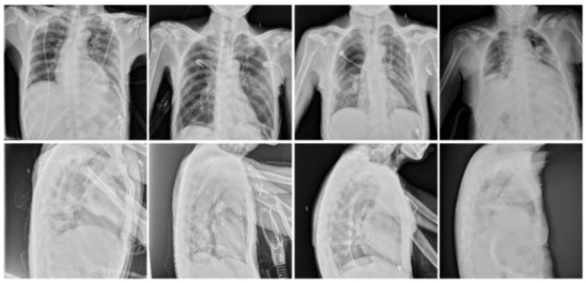

FIGURE 1. An example of the chest X-ray images of one patient from the Haut-NY dataset. The first line includes four frontal chest X-ray images. The second line contains four lateral chest X-ray images.

2) IMAGE AND METHOD ENHANCEMENTS

Data preprocessing: First, Pydicom was used to convert all DICOM files into PNG files. The original image resolution was 3200 × 3200 pixels. We zoomed in on the image to achieve a 224 × 224 pixel resolution. The advantage of this resolution is that relatively few model parameters are required and a fast training speed can be achieved. In addition, we also attempted to use resolutions of 768 × 768 and 1024 × 1024 pixels. We used bilinear interpolation [31], [32] to ensure the quality of the reduced image as much as possible.

Considering the limited number of chest X-ray images, we used the Albumentations image enhancement tool, which is a fast training data enhancement library for OpenCV, to enhance the image. It has a very simple and powerful interface that can be used for various tasks, such as classification, segmentation, and detection. In addition, it is easy to customize and add other frameworks and can be used to convert the dataset pixel by pixel. The specific image enhancement methods we used are shown in Table 2.

Because our model needs to fuse chest X-ray images of two different views of the same patient (i.e., frontal and lateral views), the data enhancement of the two images must be consistent. Otherwise, convergence cannot occur in our deep learning model.

TABLE 2. The image enhancement methods used in this experiment are as follows. The parameter "p" represents probability. For example, the probability of "blur" is 0.8, and the probability of no "blur" is 0.2. For the training dataset, we used nine methods to increase the model's generalization ability. For the test dataset, only the normalization method was used because for a real diagnosis, medical images will not be rotated or blurred.

Method	Related parameters	
RandomGamma	gamma_limit=(60, 120)	p=0.5
RandomBrightness	limit=0.2	p=0.8
RandomContrast	limit=0.2	p=0.8
Blur	blur_limit=4	p=0.8
MotionBlur	blur_limit=4	p=0.8
HorizontalFlip		p=0.5
CLAHE	clip_limit=4.0 tile_grid_size=(4, 4)	p=0.8
ShiftScaleRotate	shift_limit=0.2 scale_limit=0.2 rotate_limit=20	p=0.5
Normalize	mean=(0.485, 0.456, 0.406) std=(0.229, 0.224, 0.225) max_pixel_value=255.0	p=1

C. EVALUATED INDICATORS

True positive (TP): Positive samples are correctly classified by the model;

False negative (FN): Positive samples are incorrectly classified by the model;

False positive (FP): Negative samples are incorrectly classified by the model;

True negative (TN): Negative samples are correctly classified by the model;

The area under the curve (AUC) is defined as the area under the ROC curve. Researchers often use the AUC value as the evaluation standard of the model because the ROC curve cannot clearly explain which classifier is better. In contrast, the classifier with a larger AUC is better.

Formulas 1-6 are the six indicators used in this experiment to evaluate the performance of the classification model.

$$Accuracy = \frac{TP + TN}{TP + TN + FP + FN} \tag{1}$$

$$Recall = \frac{TP}{TP + FN} \tag{2}$$

$$Precision = \frac{TP}{TP + FP} \tag{3}$$

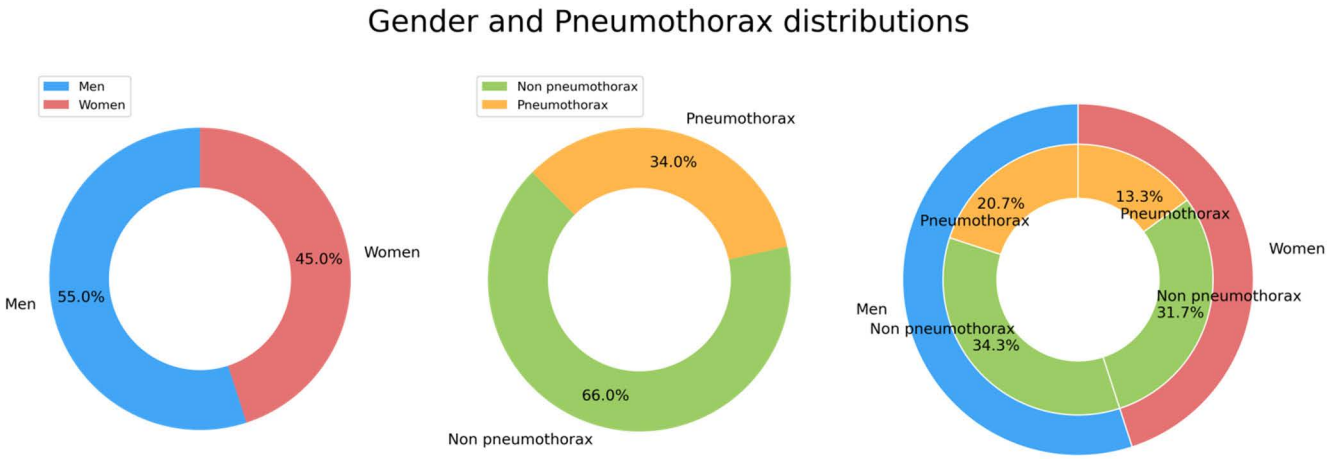

FIGURE 2. The distribution of sex and pneumothorax for the Haut-NY dataset.

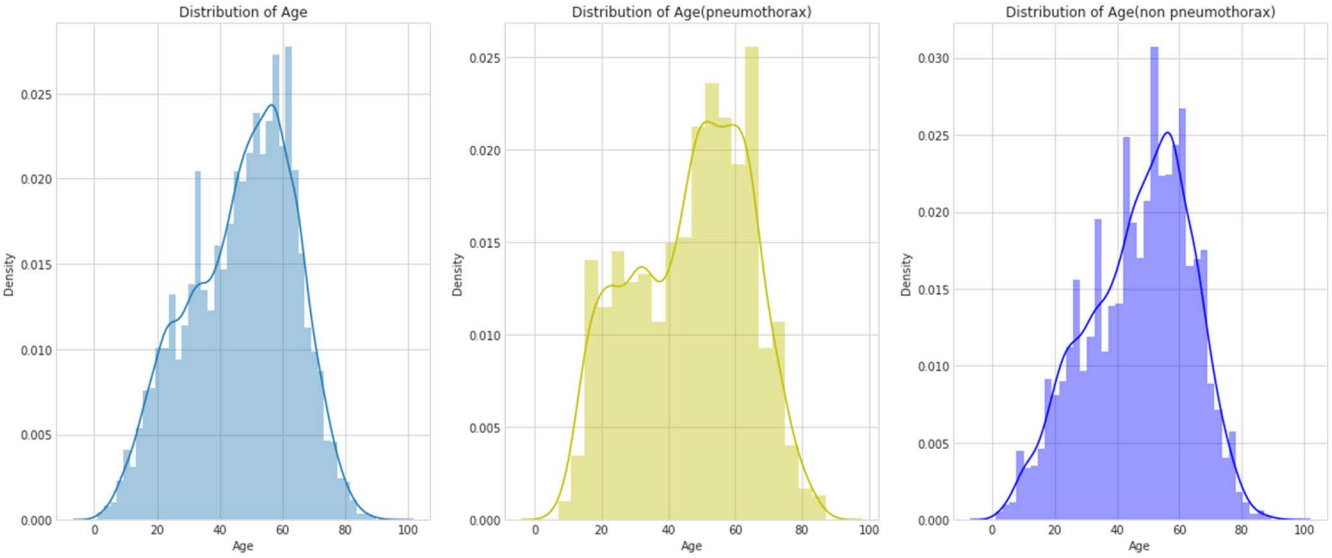

FIGURE 3. Age distribution for the Haut-NY dataset.

$$Macro\ avg = \frac{P\_no + P\_yes}{2} \tag{4}$$

$$F1 - Score = 2 \times \frac{Precision \times Reacll}{Precision + Reacll} \tag{5}$$

$$Weighted\ avg = p\_no \times (support\_no \div support\_all) + p\_yes \times (support\_yes \div support\_all) \tag{6}$$

D. SINGLE INPUT MODEL

In this experiment, we only used 2,530 frontal chest X-ray images. The label of the positive pneumothorax image is set to 1, and the negative pneumothorax image is set to 0. The model only used the frontal branch (i.e., single input, single output), as shown in Figure 6, to input the frontal chest X-ray images and output the binary classification results. We attempted to use different pretraining networks. We found that ResNet-50 always achieved the highest accuracy (Table 3). Therefore, we used ResNet-50 pretrained on ImageNet as the backbone. The input size was 224 * 224 * 3. The data were flattened using the flattening layer. Then, the image information was parsed using four fully connected layers with the ReLU activation function. The parameter of the final fully connected layers was 2 (representing the binary classification), and the softmax activation function was used to convert the output value of the binary classification into probability distributions in the range of [0,1]. The loss function was binary cross-entropy.

After the first set of experiments, we used only 2,530 lateral chest X-ray images for the next experiment. The model

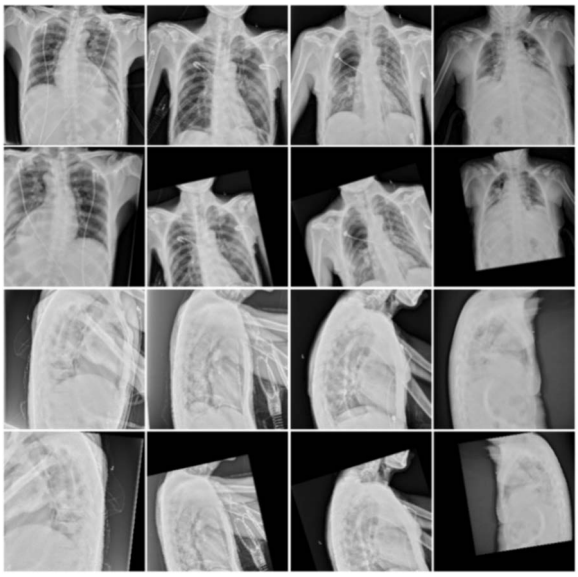

FIGURE 4. An example of chest X-ray images of a patient from the Haut-NY dataset. The first row shows the original frontal chest X-ray images, and the second row shows the frontal chest X-ray images after image enhancement. The third row shows the original lateral chest X-ray images, and the fourth row shows the lateral chest X-ray images after image enhancement. A consistent data enhancement method must be maintained for a pair of images (i.e., the frontal and lateral chest X-ray images of the same patient).

only used the lateral branches (i.e., single input and single output), as shown in Figure 6, to input the lateral chest X-ray images and output the binary classification results. The training details of the model were consistent with the previous single input single output forward chest X-ray image model.

E. MULTI-INPUT MODEL

Different from traditional learning only through frontal chest X-ray images or lateral X-ray images, we wanted to design a multi-input network that could integrate frontal chest X-ray image and chest lateral X-ray image information to diagnose pneumothorax. The model pretrained on ImageNet was used as a tool to extract image features. We attempted to use several different pretraining models as the backbone. We found that when ResNet-50 was used as the backbone, the model's accuracy was the highest (Table 6). We also found that the characteristics of the ResNet-50 network determine the accuracy. In training the model, we found that one of the challenges is the vanishing gradient problem [33], which occurs when the network is deep. The deeper the network is, the more obvious the vanishing gradient, and the poorer the training effect of the network. However, the shallow network cannot significantly improve network performance. This is a contradictory problem, but the residual block [34] (an important module in ResNet-50.) effectively alleviates the vanishing gradient in a deeper network.

$$\frac{\partial L}{\partial X_{A_{out}}} = \frac{\partial L}{\partial X_{Din}} \frac{\partial X_{Din}}{\partial X_{A_{out}}} \tag{7}$$

$$X_{Din} = X_{A_{out}} + C(B(X_{A_{out}})) \tag{8}$$

$$\frac{\partial L}{\partial X_{A_{out}}} = \frac{\partial L}{\partial X_{Din}}[1 + \frac{\partial X_{Din}}{\partial X_C} \frac{\partial X_C}{\partial X_B} \frac{\partial X_B}{\partial X_{A_{out}}}] \tag{9}$$

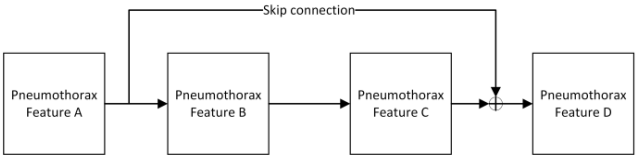

FIGURE 5. Skip connection in the residual network.

Figure 5 and Formulas 7-9 show how this is achieved. Even if the gradient attenuation occurs in the backward propagation of A-B-C, the gradient at D can still be directly transmitted to A, that is, the cross-layer propagation of the gradient is realized. From the perspective of gradient size, no matter how deep the network structure is, the residual network can maintain a large value of the weight close to the data layer (input) to alleviate the vanishing gradient.

The channel of our fusion model is deep (with a large number of feature maps). Different feature maps have different importances for pneumothorax recognition. Therefore, we decided to introduce a channel attention mechanism to optimize the model. We use the channel attention mechanism SeNet [35]. After the emergence of SeNet, the loss caused by the different importance of different channels of feature maps in the process of convolution pooling was solved. The squeeze and exception (SE) block improves the representation ability of the network by modeling the dependence of each channel and adjusts the features channel by channel so that the network can learn to selectively strengthen the features containing useful information and suppress useless features through global information.

The basic structure of SeNet is shown in Figure 7. The parameter V_C represents the C^{th} convolution kernel, and X^S represents the S^{th} input. The F_{tr} parameter represents the convolution operation before the attention mechanism, and F_{sq} represents the squeeze operation. After global average pooling, the characteristic information changes from H * W * C to 1 * 1 * C. The F_{ex} parameter represents the excitation operation. After the first fully connected layer, the ReLU layer, the characteristic information changes from 1 * 1 * C to 1 * 1 * C/r, where r is 16. After passing through the second fully connected layer and sigmoid function, the characteristic information changes from 1 * 1 * C/r to 1 * 1 * C (called weight s). The F_{scale} parameter represents the multiplication of "weights" and "U" obtained in the front convolution to obtain the output. The relevant equations of the channel attention mechanism are as follows:

$$u_c = v_c * X = \sum_{S=1}^{C'} V_c^s * X^s \tag{10}$$

$$z_c = F_{sq}(u_c) = \frac{1}{H \times W} \sum_{i=1}^{H} \sum_{j=1}^{W} u_c(i, j) \tag{11}$$

$$s = F_{ex}(z, W) \tag{12}$$

$$\tilde{X}_c = F_{scale}(u_c, s_c) \tag{13}$$

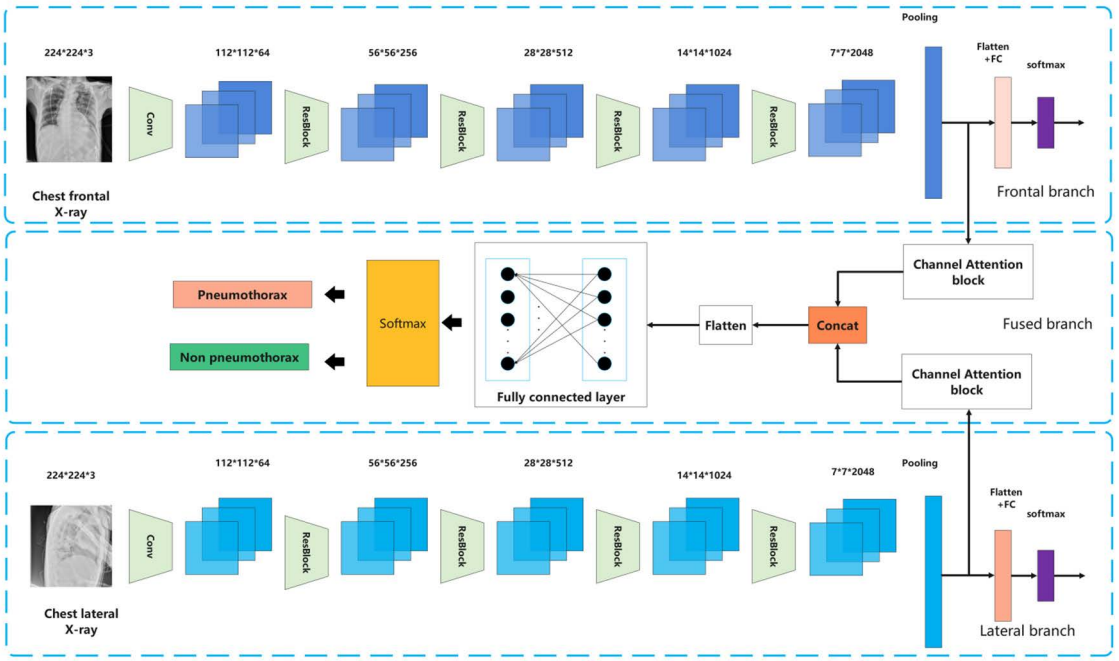

FIGURE 6. Pneumothorax recognition neural network based on feature fusion.

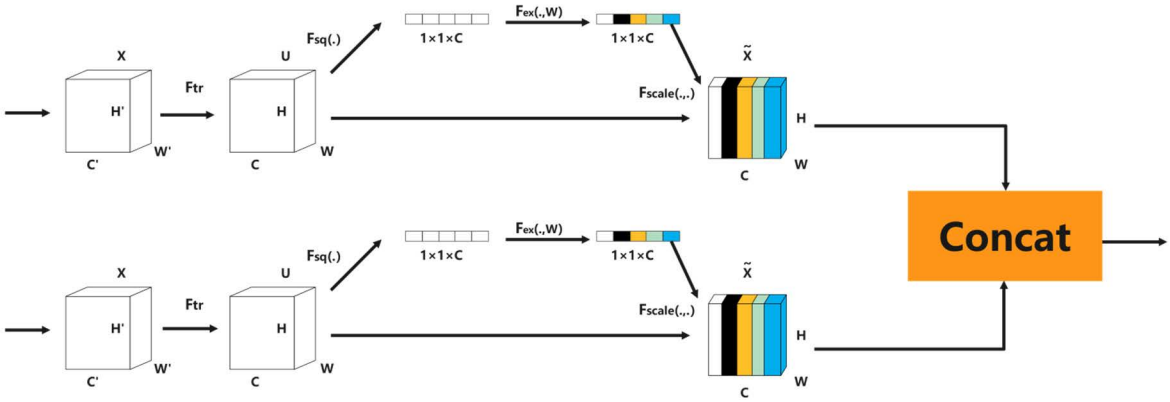

FIGURE 7. Squeeze-and-excitation module and concat.

In our work, frontal and lateral chest X-ray images were combined and two-channel attention mechanisms were used. In the first step, the global spatial characteristics of each channel were taken by the squeeze operation as the representation of the channel to form a channel descriptor. In the second step, the dependence on each channel was learned and the feature map was adjusted according to the dependence. The modified feature map was the output of the SE block. The benefits of SE block reprofiling could be accumulated throughout the network. The concat function was used to fuse information of frontal and lateral chest X-ray images, and finally, a flatten layer was used to flatten the data. Fully connected layers (FCs) played the role of classifiers in the whole convolutional neural network. Finally, the binary classification results were output using the softmax function (Formula 14).

$$Pc = \frac{\exp(f_c)}{\sum_{i=1}^{C} \exp(f_i)} \tag{14}$$

Our model has two inputs and three outputs. The two inputs are the frontal chest X-ray image and the lateral chest X-ray image. The three outputs are the classification results of the frontal chest X-ray image, the classification results of the lateral chest X-ray image, and the classification results integrating the characteristics of the fused frontal chest X-ray image and lateral chest X-ray image. Our fusion model can fuse frontal feature maps and lateral feature maps of chest X-ray images and then learn them.

$$F_{Total} = F_{Fc}\{F_{F\ latten}[Concat(F_{F--featuremap}, F_{L--featuremap})]\} \tag{15}$$

The loss function was binary cross-entropy (Formula 16). Using cross-entropy as the loss function can alleviate the imbalance between positive and negative samples to a certain extent, and the calculated gradient is more stable [36]. The loss function adopted by the three branches was binary cross-entropy, but the weighting indices of the three branches are different (Formula 17).

$$L_{BCE} = -\sum_{i}[y_i \log(\hat{y_i}) + (1 - y_i)\log(1 - \hat{y_i})] \quad (16)$$

$$L_{Total} = \lambda_{Fused} L_{Fused\_BCE} + \lambda_{Frontal} L_{Frontal\_BCE} + \lambda_{Lateral} L_{Lateral\_BCE} \quad (17)$$

All experiments in this study adopted the 5-fold-cross-validation method, where the data were divided into five equal parts on average. Each data point was completely independent and did not cross other data points. One part of the data was taken for testing in each experiment, and the rest was used for training. The average value was obtained for five experiments.

Algorithm: 5-Fold Cross-Validation

Input: Preprocess pneumothorax dataset, then the dataset was randomly divided into 5 parts on average:

$$D = D_1 \cup D_2 \cup D_3 \cup D_4 \cup D_5$$

$$D_i \neq D_j (i \neq j)$$

1 o=1;
2 **for** $o \leq 5$ **do**
3 Train model using D − Do;
4 Test model using Do;
5 Save score as R;
7 o++;
end
Output: $\frac{\sum R}{5}$

F. EXPERIMENTAL DETAILS AND OPTIMIZATION METHODS

The following experimental hyperparameter settings were utilized. The Adam optimizer was used, the batch size was 32, and the initial learning rate was 0.0001. The epoch was 60. If the model's performance was not improved after five epochs were trained continuously, the learning rate was decreased to one-tenth of its original value. If the performance after 15 epochs was not enhanced, ''early stop'' was initiated to prevent overfitting. All networks were implemented based on the TensorFlow framework and trained using NVIDIA GeForce RTX 3080 Ti GPU cards.

G. CLASSIFICATION RESULTS

1) SINGLE INPUT MODEL CLASSIFICATION RESULTS

The classification results of frontal chest X-ray images are shown in Table 4. First, for the binary classification of the frontal images, based on the 334 nonpneumothorax images, a recognition precision of 0.89 was achieved, and based on the 172 pneumothorax images a recognition precision of 0.82 was achieved. The recognition accuracy was 0.87.

The classification results of lateral chest X-ray images are shown in Table 5. First, for the binary classification of the frontal images, based on the 334 nonpneumothorax images, a recognition precision of 0.90 was achieved, and based on the 172 pneumothorax images, a recognition precision of 0.77 was achieved. The recognition accuracy was 0.85.

TABLE 3. Prediction results of single input models under different pretraining networks. (AUC was the indicator.)

Pretraining model	AUC
Resnet50 (frontal image)	**0.932**
Resnet50 (lateral image)	**0.924**
VGG16 (frontal image)	0.918
VGG16 (lateral image)	0.920
EfficientNet-b4 (frontal image)	0.924
EfficientNet-b4 (lateral image)	0.924
Inceptionv3 (frontal image)	0.922
Inceptionv3 (lateral image)	0.919
Inceptionv4 (frontal image)	0.930
Inceptionv4 (lateral image)	0.923
DenseNet-121 (frontal image)	0.931
DenseNet-121 (lateral image)	0.923

2) MULTI-INPUT MODEL CLASSIFICATION RESULTS

For the case of multiple inputs, the classification results of the frontal branch are shown in Table 7. For the 334 images from patients without pneumothorax, a recognition precision of 0.93 was achieved, and for the 172 images from patients with pneumothorax, a recognition precision of 0.85 was achieved. The recognition accuracy was 0.91. In the case of multiple inputs, the classification results of the lateral branch are shown in Table 8. For the 334 images from patients without pneumothorax, a recognition precision of 0.91 was achieved, and for the 172 images from patients with pneumothorax, a recognition precision of 0.87 was achieved. The recognition accuracy was 0.90. Compared with a single input, all values were improved to varying degrees.

The most obvious improvement in the accuracy was a result of the fusion branch. In the case of multiple inputs (without channel attention), the classification results of the frontal branch are shown in Table 9. For the 334 images from patients without pneumothorax, a recognition precision of 0.95 was achieved, and for the 172 images from patients with pneumothorax, a recognition precision of 0.88 was achieved. The recognition accuracy was 0.92. Both the macro avg and weighted avg indices improved to varying degrees. In the case of combining the multiple inputs model and channel attention, the classification results of the frontal branch are shown in Table 10. For the 334 images from patients without pneumothorax, a recognition precision of 0.93 was achieved, and for the 172 images from patients with pneumothorax, a recognition precision of 0.95 was achieved. The recognition accuracy was 0.94. Both macro avg and weighted avg indices improved to varying degrees.

TABLE 4. Comprehensive performance index of the pneumothorax binary classification for frontal chest X-ray images (single input, single output).

	Precision	Recall	F1-score	Number
Nonpneumothorax	0.89	0.91	0.90	334
Pneumothorax	0.82	0.79	0.81	172
Accuracy			0.87	506
Macro avg	0.86	0.85	0.86	506
Weighted avg	0.87	0.87	0.87	506

TABLE 5. Comprehensive performance index of the pneumothorax binary classification for lateral chest X-ray images (single input, single output).

	Precision	Recall	F1-score	Number
Nonpneumothorax	0.90	0.87	0.89	334
Pneumothorax	0.77	0.81	0.79	172
Accuracy			0.85	506
Macro avg	0.83	0.84	0.84	506
Weighted avg	0.85	0.85	0.85	506

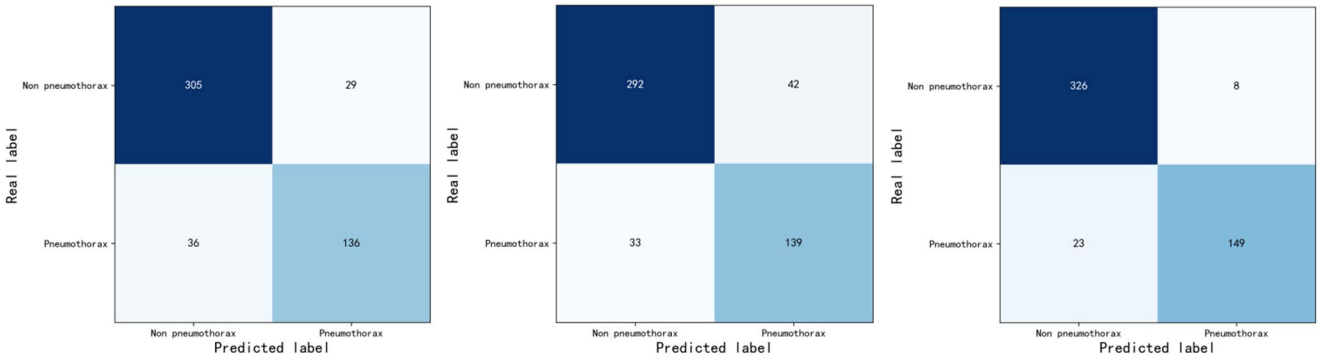

FIGURE 8. Pneumothorax classification confusion matrix of the frontal images (Single input), lateral images (Single input) and fused branch (With channel attention).

TABLE 6. Prediction results of multi-input models under different pretraining networks. (AUC was the indicator.)

Pretraining model	AUC
Resnet50 (frontal branch)	**0.956**
Resnet50 (lateral branch)	**0.950**
Resnet50 (fused branch)	**0.975**
VGG16 (frontal branch)	0.940
VGG16 (lateral branch)	0.941
VGG16 (fused branch)	0.958
EfficientNet-b4 (frontal branch)	0.952
EfficientNet-b4 (lateral branch)	0.943
EfficientNet-b4 (fused branch)	0.961
Inceptionv3 (frontal branch)	0.952
Inceptionv3 (lateral branch)	0.947
Inceptionv3 (fused branch)	0.959
Inceptionv4 (frontal branch)	0.955
Inceptionv4 (lateral branch)	0.948
Inceptionv4 (fused branch)	0.972
DenseNet-121 (frontal branch)	0.956
DenseNet-121 (lateral branch)	0.948
DenseNet-121 (fused branch)	0.974

H. SOME FACTORS AFFECTING THE ACCURACY OF THE MODEL

1) INFLUENCE OF MODEL TRAINING SEQUENCE ON ACCURACY

We also found that training three branches in different sequences will affect the performance of the fusion model. We trained our fusion model with four different sequences.

1) Three branches were trained at the same time (train together).
2) First, the frontal branch was trained, and then the lateral branch and fused branch were trained (1-2-3).
3) First, the lateral branches were trained, and then the frontal branch and fused branch were trained (2-1-3).
4) The frontal and lateral branches were trained together, and then fused branch was trained (1 2-3)

2) INFLUENCE OF WEIGHT RATIO OF LOSS FUNCTION ON MODEL ACCURACY

Because our model contains three outputs, the weight ratio between the three loss functions must be considered. In fact, in our experiment, different weight ratios affect the accuracy of the model to a certain extent.

We found that when the weight of the loss function is set to 1:0.6:0.6 (fused:frontal:lateral), the fused branch achieved the highest AUC.

I. STATISTICAL ANALYSIS OF THE FUSION MODEL

We attempted to analyze the connection between the frontal branch, lateral branch, and fusion branch from the perspective of statistics. Softmax was used in the process of binary

TABLE 7. The comprehensive performance index of the pneumothorax binary classification for frontal chest X-ray images (two inputs, three outputs).

	Precision	Recall	F1-score	Number
Nonpneumothorax	0.93	0.92	0.93	334
Pneumothorax	0.85	0.87	0.86	172
Accuracy			0.91	506
Macro avg	0.89	0.90	0.89	506
Weighted avg	0.91	0.91	0.91	506

TABLE 8. The comprehensive performance index of the pneumothorax binary classification for lateral chest X-ray images (two inputs, three outputs).

	Precision	Recall	F1-score	Number
Nonpneumothorax	0.91	0.94	0.92	334
Pneumothorax	0.87	0.83	0.85	172
Accuracy			0.90	506
Macro avg	0.89	0.88	0.89	506
Weighted avg	0.90	0.90	0.90	506

TABLE 9. The comprehensive performance index of the pneumothorax binary classification for fused images (two inputs, three outputs, and without channel attention).

	Precision	Recall	F1-score	Number
Nonpneumothorax	0.95	0.94	0.94	334
Pneumothorax	0.88	0.90	0.89	172
Accuracy			0.92	506
Macro avg	0.91	0.92	0.92	506
Weighted avg	0.93	0.92	0.93	506

TABLE 10. The comprehensive performance index of the pneumothorax binary classification for fused images (two inputs, three outputs, and with channel attention).

	Precision	Recall	F1-score	Number
Nonpneumothorax	0.93	0.98	0.95	334
Pneumothorax	0.95	0.87	0.91	172
Accuracy			0.94	506
Macro avg	0.94	0.92	0.93	506
Weighted avg	0.94	0.94	0.94	506

TABLE 11. Area under the curve (AUC), 95% confidence interval (CI), and convergence time with different strategies.

Method	Mean AUC (95%CI)	Mean Convergence Time
(1) Frontal chest X-ray image (Single input model)	0.932 (0.928-0.935)	5.5 hours
(2) Lateral chest X-ray image (Single input model)	0.924 (0.921-0.927)	5.7 hours
(3) Frontal chest X-ray image (Frontal branch)	0.956 (0.953-0.959)	10.3 hours
(4) Lateral chest X-ray image (Lateral branch)	0.950 (0.948-0.952)	10.2 hours
(5) Feature fusion (Fused branch)	0.962 (0.958-0.964)	10.7 hours
(6) **Feature fusion + Channel attention (Fused branch)**	0.975 (0.974-0.977)	11.1 hours

classification to map the output of multiple neurons into the (0,1) interval, which can be understood as probability, to carry out binary classification when we input a chest X-ray image into the model. The softmax function output of the frontal branch was [0.49,0.51], which means that the probability of the corresponding chest X-ray image showing nonpneumothorax is 0.49, and the probability of pneumothorax is 0.51. The softmax function output of the lateral branch is [0.01,0.99], which means that the probability that the lateral branch assesses the corresponding chest X-ray image is nonpneumothorax is 0.01, and the probability of pneumothorax is 0.99.

Let the softmax function output of the frontal branch be $[X_{Frontal}, Y_{Frontal}]$, the softmax function output of the

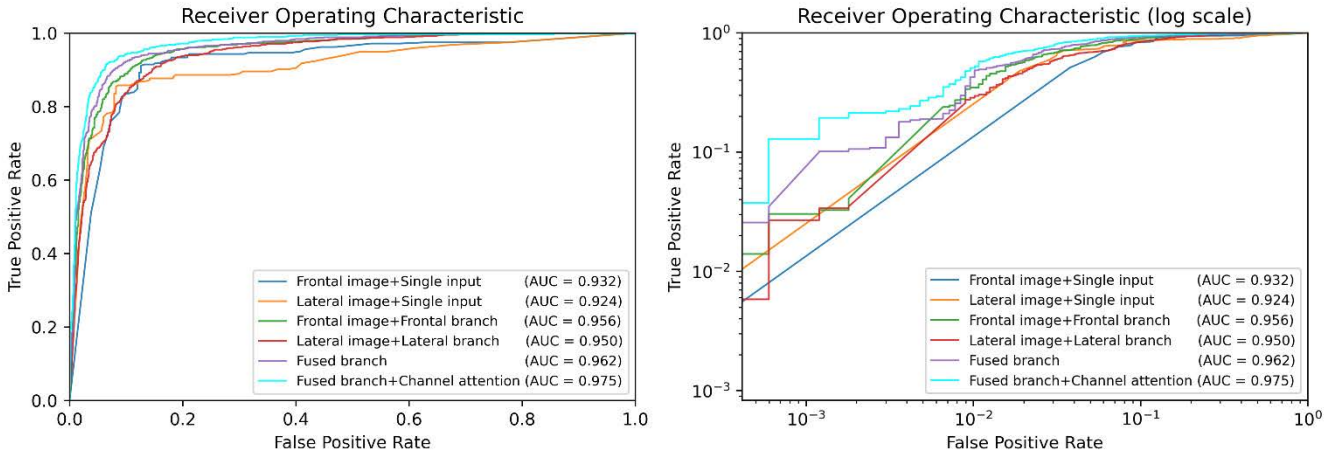

FIGURE 9. The ROC curves of all methods (corresponding to Table 11).

TABLE 12. AUC under different training sequences. (ResNet-50 was used as the backbone.)

Training sequence	Frontal branch (1)	Lateral Branch (2)	Fused branch (3)
Train together	**0.956**	**0.950**	**0.975**
1-2-3	0.960	0.949	0.971
2-1-3	0.953	0.954	0.969
1 2-3	0.952	0.955	0.973

TABLE 13. AUC under different training weight ratios. (ResNet-50 was used as the backbone, and the training sequence was trained together.)

Weight ratio (Fused: Frontal: Lateral)	Frontal branch	Lateral branch	Fused branch
1:0.2:0.2	0.906	0.892	0.951
1:0.4:0.4	0.906	0.896	0.960
1:0.6:0.6	**0.956**	**0.950**	**0.975**
1:0.8:0.8	0.959	0.955	0.963
1:1:1	0.955	0.956	0.959

lateral branch be [$X_{Lateral}$, YLateral], and the softmax function output of the fusion branch be [X_{Fused}, Y_{Fused}]. The connection between the three is shown in Table 14, where P (YFused $>$ 0.5) represents the probability that the corresponding image of fusion branch recognition is positive pneumothorax.

IV. COMPARISON WITH OTHER WORK

Relevant articles from recent years on pneumothorax classification were divided into two categories. The first category was multiclassification, which usually predicts 5-14 different chest diseases, and the AUC for pneumothorax recognition ranges from 0.80 to 0.92 [19], [26], [39]–[41].

TABLE 14. The relationship between the activation functions of the three branches.

$Y_{Frontal}+Y_{Lateral}$	P ($Y_{Fused>0.5}$)
(0-0.02]	0
(0.02-0.2]	0.08
(0.2-0.4]	0.21
(0.4-0.6]	0.36
(0.6-0.8]	0.44
(0.8-1.0]	0.63
(1.0-1.2]	0.89
(1.2-1.4]	0.92
(1.4-1.6]	0.95
(1.6-1.8]	0.97
(1.8-2.0)	0.99

The second category of articles was the binary classification of pneumothorax [14], [37], [38]. The work related to the binary classification of pneumothorax was the main comparison for this experiment.

Taylor *et al.* [37] established a private pneumothorax dataset. They used several different pretraining networks for comparative experiments. The average AUC obtained in pneumothorax detection was 0.94. Their main contribution was to analyze the differences in recognizing various severities of pneumothorax, such as nonpneumothorax, trace pneumothorax, moderate or large pneumothorax. In the case of unbalanced pneumothorax datasets, Wang Y *et al.* [38] used the positive image augmentation method to increase the positive pneumothorax cases and improve recognition accuracy. When the ratio of the original positive pneumothorax sample to the negative pneumothorax sample was 1507:26891, the model's accuracy was only 50.08%. Then, they increased the data of positive pneumothorax cases to 27126:26891 (no new positive images were added, only image augmentation was used), and the model's accuracy improved to 88.52%.

TABLE 15. Comparison with the work of other researchers in recent years (binary classification of pneumothorax).

Articles	Datasets and details	Methods	Image size	AUC	Accuracy	Precision	Recall	F1-score
Taylor et al.[37] (2018)	Private dataset Image level annotation Only frontal images	VGG19 Inception ResNet Xception	512*512 512*512 512*512 512*512	0.94	---	---	---	---
Wang Y et al.[38] (2019)	Private dataset+ChestX-ray14 Image level annotation Only frontal images	VGG16 VGG16 + image augmentation ChestNet + image augmentation	480*480 480*480 480*480	--- --- 0.9906	0.5008 0.8852 0.9451	--- --- ---	--- --- ---	--- --- ---
X. Wang et al.[14] (2020)	SIIM-ACR Pixel-level annotation Only frontal images	Multitask+EfficientNet-B3 Multitask+SE-ResNext50 Multitask+SE-ResNext50	1024*1024 1024*1024 768*768	0.9748 0.9786 0.9763	0.9417 0.9467 0.9446	0.8103 0.8206 0.8068	0.9038 0.9189 0.9212	0.8545 0.8670 0.8601
This article	Haut-NY (Private dataset) Image level annotation Frontal image + Lateral image	**Fusion model** **Fusion model** **Fusion model**	**224*224** **768*768** **1024*1024**	**0.975** **0.977** **0.979**	**0.943** **0.944** **0.948**	**0.951** **0.932** **0.925**	**0.873** **0.897** **0.908**	**0.910** **0.914** **0.916**

However, only using image augmentation to expand the positive samples may risk overfitting without adding new images. It may only improve the recognition accuracy of the current dataset, while in the face of new datasets, the recognition accuracy of the model may be reduced. The strategy by X. Wang *et al.* [14] was to use pixel-level pneumothorax annotation combined with a multitask learning model to achieve high-precision pneumothorax classification. Their work was very comprehensive. Among the five evaluated indicators in Table 15, AUC is the most valuable because AUC can resist the imbalance of the number of samples to a certain extent. The accuracy, precision, recall, and F1-score are vulnerable to data imbalance (i.e., the number of positive and negative pneumothorax cases).

V. DISCUSSION

When accuracy was the evaluated indicator, using the fusion network improved the accuracy by approximately 7% compared with using only the frontal chest X-ray image information and approximately 9% more accurate than using only lateral chest X-ray image information. When AUC was the evaluated indicator, our fusion model was 4% higher than that using only frontal or lateral models. In fact, by comparing the data in Table 11, we found that no matter which performance index was used as the evaluation, the performance of the fusion network was the best.

Our further experiments showed that the accuracy of pneumothorax recognition was related to the training sequence of the model and the weight ratio of the loss function. When the training sequence was three branches trained simultaneously and the weight of the loss function was 1:0.6:0.6 (fused:frontal: lateral), the model's accuracy was the highest.

Referring to Table 15, using only image-level annotation, our model still achieved high pneumothorax recognition accuracy.

VI. CONCLUSION AND FUTURE DIRECTIONS

We proposed a pneumothorax binary classification neural network based on feature fusion. This was meaningful because most of the literature on pneumothorax recognition only considers frontal chest X-ray images. Our model could be used to fuse frontal and lateral X-ray information to achieve higher precision pneumothorax recognition. The model design considered the phenomenon of the vanishing gradient in deeper neural networks, so we introduced the residual block to alleviate it. There were too many channels in the feature map after feature fusion, so the channel attention mechanism SeNet was used to adjust the feature map. Comparative experiments showed that the accuracy of this method was higher than that of the traditional single task pneumothorax recognition network. The main value of our work is that only using image-level datasets can achieve high pneumothorax recognition accuracy. However, we need pairs of image-level annotations (frontal annotation + lateral annotation) rather than only front images. Therefore, our dataset is more expensive than the dataset containing only frontal images. This is a limitation of our method. However, the cost is still lower than that of pixel-level annotations, even for paired image-level annotations. Therefore, the proposed method may assist radiologists with the prompt and accurate diagnosis of pneumothorax and precise treatment planning.

Future work is as follows. First, we will improve the dataset, expand the number of images, invite experienced radiologists to add pixel-level annotations to our dataset, and conduct in-depth research around visualization techniques. Second, we will combine our model with the expert system [42] and the fuzzy consensus [43], which play an important role in artificial intelligence-aided diagnosis and the internet of medical things.

ACKNOWLEDGMENT

The authors would like to thank the Nanyang Central Hospital for providing them with the dataset.

REFERENCES

[1] K.-M. Yeow, I.-H. Su, K.-T. Pan, P.-K. Tsay, K.-W. Lui, Y.-C. Cheung, and A. S.-B. Chou, "Risk factors of pneumothorax and bleeding: Multivariate analysis of 660 CT-guided coaxial cutting needle lung biopsies," *Chest*, vol. 126, no. 3, pp. 748–754, 2004.

[2] M. Blaivas, M. Lyon, and S. Duggal, "A prospective comparison of supine chest radiography and bedside ultrasound for the diagnosis of traumatic pneumothorax," *Academic Emergency Med.*, vol. 12, no. 9, pp. 844–849, Sep. 2005.
[3] T. Roth, M. Alifano, O. Schussler, P. Magdaleinat, and J.-F. Regnard, "Catamenial pneumothorax: Chest X-ray sign and thoracoscopic treatment," *Ann. Thoracic Surg.*, vol. 74, no. 2, pp. 563–565, Aug. 2002.
[4] A. J. Salazar, D. A. Aguirre, J. Ocampo, J. C. Camacho, and X. A. Díaz, "Evaluation of three pneumothorax size quantification methods on digitized chest X-ray films using medical-grade grayscale and consumer-grade color displays," *J. Digit. Imag.*, vol. 27, no. 2, pp. 280–286, Apr. 2014.
[5] K. Suzuki, L. Feng, S. Sone, and K. Doi, "Computer-aided diagnostic scheme for distinction between benign and malignant nodules in thoracic low-dose CT by use of massive training artificial neural network," *IEEE Trans. Med. Imag.*, vol. 24, no. 9, pp. 1138–1150, Sep. 2005.
[6] S. Sanada, K. Doi, and H. Macmahon, "Image feature analysis and computer-aided diagnosis in digital radiography: Automated detection of pneumothorax in chest images," *Med. Phys.*, vol. 19, no. 5, pp. 1153–1160, Sep. 1992.
[7] J. Gao, J. Yang, J. Zhang, and M. Li, "Natural scene recognition based on convolutional neural networks and deep Boltzmannn machines," in *Proc. IEEE Int. Conf. Mechatronics Autom. (ICMA)*, Aug. 2015, pp. 2369–2374.
[8] D. Polap, N. Wawrzyniak, and M. Wlodarczyk-Sielicka, "Side-scan sonar analysis using ROI analysis and deep neural networks," *IEEE Trans. Geosci. Remote Sens.*, vol. 60, pp. 1–8, 2022.
[9] L. Wang, C. Wang, Z. Sun, and S. Chen, "An improved dice loss for pneumothorax segmentation by mining the information of negative areas," *IEEE Access*, vol. 8, pp. 167939–167949, 2020.
[10] S. Bharati, P. Podder, and M. R. H. Mondal, "Hybrid deep learning for detecting lung diseases from X-ray images," *Informat. Med. Unlocked*, vol. 20, Jan. 2020, Art. no. 100391.
[11] V. Badrinarayanan, A. Kendall, and R. Cipolla, "SegNet: A deep convolutional encoder-decoder architecture for image segmentation," *IEEE Trans. Pattern Anal. Mach. Intell.*, vol. 39, no. 12, pp. 2481–2495, Dec. 2017.
[12] D. A. Moses, "Deep learning applied to automatic disease detection using chest X-rays," *J. Med. Imag. Radiat. Oncol.*, vol. 65, no. 5, pp. 498–517, Aug. 2021.
[13] M. Yahyatabar, P. Jouvet, and F. Cheriet, "Dense-UNet: A light model for lung fields segmentation in chest X-ray images," in *Proc. 42nd Annu. Int. Conf. IEEE Eng. Med. Biol. Soc. (EMBC)*, Jul. 2020, pp. 1242–1245.
[14] X. Wang, S. Yang, J. Lan, Y. Fang, J. He, M. Wang, J. Zhang, and X. Han, "Automatic segmentation of pneumothorax in chest radiographs based on a two-stage deep learning method," *IEEE Trans. Cogn. Develop. Syst.*, vol. 14, no. 1, pp. 205–218, Mar. 2022.
[15] Y. Zhang and Q. Yang, "A survey on multi-task learning," *IEEE Trans. Knowl. Data Eng.*, early access, Mar. 31, 2021, doi: 10.1109/TKDE.2021.3070203.
[16] A. Malhotra, S. Mittal, P. Majumdar, S. Chhabra, K. Thakral, M. Vatsa, R. Singh, S. Chaudhury, A. Pudrod, and A. Agrawal, "Multi-task driven explainable diagnosis of COVID-19 using chest X-ray images," *Pattern Recognit.*, vol. 122, Feb. 2022, Art. no. 108243.
[17] M. Shorfuzzaman and M. S. Hossain, "MetaCOVID: A Siamese neural network framework with contrastive loss for n-shot diagnosis of COVID-19 patients," *Pattern Recognit.*, vol. 113, May 2021, Art. no. 107700.
[18] K. He, C. Lian, B. Zhang, X. Zhang, X. Cao, D. Nie, Y. Gao, J. Zhang, and D. Shen, "HF-UNet: Learning hierarchically inter-task relevance in multi-task U-Net for accurate prostate segmentation in CT images," *IEEE Trans. Med. Imag.*, vol. 40, no. 8, pp. 2118–2128, Aug. 2021.
[19] X. Wang, Y. Peng, L. Lu, Z. Lu, M. Bagheri, and R. M. Summers, "ChestX-ray8: Hospital-scale chest X-ray database and benchmarks on weakly-supervised classification and localization of common thorax diseases," in *Proc. IEEE Conf. Comput. Vis. Pattern Recognit. (CVPR)*, Jul. 2017, pp. 2097–2106.
[20] *NIH Chest X-Rays*. Accessed: 2018. [Online]. Available: https://www.kaggle.com/nih-chest-xrays/data
[21] *SIIM-ACR Pneumothorax Segmentation*. Accessed: 2019. [Online]. Available: https://www.kaggle.com/c/siim-acr-pneumothorax-segmentation
[22] O. Geva, G. Zimmerman-Moreno, S. Lieberman, E. Konen, and H. Greenspan, "Pneumothorax detection in chest radiographs using local and global texture signatures," *Proc. SPIE*, vol. 9414, Mar. 2015, Art. no. 94141P.
[23] Y.-H. Chan, Y.-Z. Zeng, H.-C. Wu, M.-C. Wu, and H.-M. Sun, "Effective pneumothorax detection for chest X-ray images using local binary pattern and support vector machine," *J. Healthcare Eng.*, vol. 2018, pp. 1–11, Apr. 2018.
[24] G. Kitamura and C. Deible, "Retraining an open-source pneumothorax detecting machine learning algorithm for improved performance to medical images," *Clin. Imag.*, vol. 61, pp. 15–19, May 2020.
[25] R. W. Filice, A. Stein, C. C. Wu, V. A. Arteaga, S. Borstelmann, R. Gaddikeri, M. Galperin-Aizenberg, R. R. Gill, M. C. Godoy, S. B. Hobbs, J. Jeudy, P. C. Lakhani, A. Laroia, S. M. Nayak, M. R. Parekh, P. Prasanna, P. Shah, D. Vummidi, K. Yaddanapudi, and G. Shih, "Crowdsourcing pneumothorax annotations using machine learning annotations on the NIH chest X-ray dataset," *J. Digit. Imag.*, vol. 33, no. 2, pp. 490–496, Apr. 2020.
[26] M. Cicero, A. Bilbily, E. Colak, T. Dowdell, B. Gray, K. Perampaladas, and J. Barfett, "Training and validating a deep convolutional neural network for computer-aided detection and classification of abnormalities on frontal chest radiographs," *Invest. Radiol.*, vol. 52, no. 5, pp. 281–287, 2017.
[27] A. G. Taylor, C. Mielke, and J. Mongan, "Automated detection of moderate and large pneumothorax on frontal chest X-rays using deep convolutional neural networks: A retrospective study," *PLOS Med.*, vol. 15, no. 11, Nov. 2018, Art. no. e1002697.
[28] P. Rajpurkar *et al.*, "Deep learning for chest radiograph diagnosis: A retrospective comparison of the CheXNeXt algorithm to practicing radiologists," *PLOS Med.*, vol. 15, no. 11, Nov. 2018, Art. no. e1002686.
[29] S. Park, S. M. Lee, N. Kim, J. Choe, Y. Cho, K.-H. Do, and J. B. Seo, "Application of deep learning–based computer-aided detection system: Detecting pneumothorax on chest radiograph after biopsy," *Eur. Radiol.*, vol. 29, no. 10, pp. 5341–5348, Oct. 2019.
[30] X. Wang, Y. Peng, L. Lu, Z. Lu, and R. M. Summers, "TieNet: Text-image embedding network for common thorax disease classification and reporting in chest X-rays," in *Proc. IEEE CVPR*, Jun. 2018, pp. 9049–9058.
[31] E. J. Kirkland, "Bilinear interpolation," in *Advanced Computing in Electron Microscopy*. New York, NY, USA: Springer, 2010, pp. 261–263.
[32] S.-M. Guo, C.-Y. Hsu, G.-C. Shih, and C.-W. Chen, "Fast pixel-size-based large-scale enlargement and reduction of image: Adaptive combination of bilinear interpolation and discrete cosine transform," *Proc. SPIE*, vol. 20, no. 3, p. 51, 2011.
[33] M. Roodschild, J. G. Sardiñas, and A. Will, "A new approach for the vanishing gradient problem on sigmoid activation," *Prog. Artif. Intell.*, vol. 9, no. 4, pp. 351–360, Dec. 2020.
[34] K. He, X. Zhang, S. Ren, and J. Sun, "Deep residual learning for image recognition," in *Proc. IEEE Conf. Comput. Vis. Pattern Recognit. (CVPR)*, Jun. 2016, pp. 770–778.
[35] J. Hu, L. Shen, S. Albanie, G. Sun, and E. Wu, "Squeeze-and-excitation networks," *IEEE Trans. Pattern Anal. Mach. Intell.*, vol. 42, no. 8, pp. 2011–2023, Aug. 2020.
[36] A. Semenov, V. Boginski, and E. L. Pasiliao, "Neural networks with multidimensional cross-entropy loss functions," in *Proc. Int. Conf. Comput. Data Social Netw.* Cham, Switzerland: Springer, 2019, pp. 57–62.
[37] A. G. Taylor, C. Mielke, and J. Mongan, "Automated detection of moderate and large pneumothorax on frontal chest X-rays using deep convolutional neural networks: A retrospective study," *PLOS Med.*, vol. 15, no. 11, Nov. 2018, Art. no. e1002697.
[38] Y. Wang, L. Sun, and Q. Jin, "Enhanced diagnosis of pneumothorax with an improved real-time augmentation for imbalanced chest X-rays data based on DCNN," *IEEE/ACM Trans. Comput. Biol. Bioinf.*, vol. 18, no. 3, pp. 951–962, May 2021.
[39] B. Chen, J. Li, X. Guo, and G. Lu, "DualCheXNet: Dual asymmetric feature learning for thoracic disease classification in chest X-rays," *Biomed. Signal Process. Control*, vol. 53, Aug. 2019, Art. no. 101554.
[40] P. Kumar, M. Grewal, and M. M. Srivastava, "Boosted cascaded convnets for multilabel classification of thoracic diseases in chest radiographs," in *Proc. Int. Conf. Image Anal. Recognit.* Cham, Switzerland: Springer, 2018, pp. 546–552.
[41] C. Yan, J. Yao, R. Li, Z. Xu, and J. Huang, "Weakly supervised deep learning for thoracic disease classification and localization on chest X-rays," in *Proc. ACM Int. Conf. Bioinf., Comput. Biol., Health Informat.*, Aug. 2018, pp. 103–110.
[42] A. Saibene, M. Assale, and M. Giltri, "Expert systems: Definitions, advantages and issues in medical field applications," *Expert Syst. Appl.*, vol. 177, Sep. 2021, Art. no. 114900.
[43] D. Połap, "Fuzzy consensus with federated learning method in medical systems," *IEEE Access*, vol. 9, pp. 150383–150392, 2021.

JIA XIN LUO was born in Henan, China, in 1996. He received the bachelor's degree from the College of Information and Business, Zhongyuan University of Technology, in 2018. He is currently pursuing the master's degree with the School of Electrical Engineering, Henan University of Technology. His research interests include machine learning, medical image processing, and computer vision.

WU FENG LIU was born in Hunan, China, in 1983. He received the Ph.D. degree in engineering from the Graduate School of the Chinese Academy of Sciences, in 2009. He was at the Institute of Modern Physics, Chinese Academy of Sciences, in 2009, where he was supported by the "light of the West" Talent Project, in 2010, and was a Senior Engineer, in 2011. He is now a Professor with the Henan University of Technology and an Academic and Technical Leader with the Henan Provincial Department of Education, engaged in medical image processing, accelerator control, and data acquisition.

LIANG YU was born in Anhui, China, in 1999. He received the bachelor's degree from the Anhui University of Science and Technology, in 2020. He is currently pursuing the master's degree with the School of Electrical Engineering, Henan University of Technology. His main research interests include deep learning, medical image processing, and computer vision.